Journal of Materials Chemistry A

ROYAL SOCIETY OF CHEMISTRY

PAPER

View Article Online
View Journal | View Issue





Cite this: J. Mater. Chem. A, 2021, 9, 23619

# Optoelectronic property comparison for isostructural $Cu_2BaGeSe_4$ and $Cu_2BaSnS_4$ solar absorbers†

Yongshin Kim, [a] Hannes Hempel,[b] Sergiu Levcenco, [b] Julie Euvrard, [a] Eric Bergmann,[c] Oki Gunawan,[d] Thomas Unold, [b] Ian G. Hill[c] and David B. Mitzi *[ae]

To target mitigation of anti-site defect formation in $Cu_2ZnSnS_{4-x}Se_x$, a new class of chalcogenides, for which Ba or Sr (group 2) replace Zn (group 12), has recently been introduced for prospective solar absorber application. $Cu_2BaGeSe_4$ (CBGSe) and $Cu_2BaSnS_4$ (CBTS) are two such compounds, which share a common trigonal crystal structure ($P3_1$ space group) and similar quasi-direct band gap (~2 eV). While CBTS-based films have already been studied, there are no reports yet on films and solar cells based on related CBGSe. To identify key differences and similarities in the electronic properties between these two materials, electronic characteristics (*e.g.*, carrier concentration, mobility, electron affinity, defect levels, recombination, and charge carrier kinetics) of vacuum-deposited CBGSe and CBTS films are compared using a variety of characterization methods. Hall effect measurements reveal that CBGSe films have relatively higher hole carrier concentration and lower mobility ($3 \times 10^{15}$ cm$^{-3}$, 0.6 cm$^2$ V$^{-1}$ s$^{-1}$) compared to CBTS ($5 \times 10^{12}$ cm$^{-3}$, 3.5 cm$^2$ V$^{-1}$ s$^{-1}$). Photoelectron spectroscopy yields low electron affinity values for both CBGSe (3.7 eV) and CBTS (3.3 eV), pointing to the necessity of pursuing low electron affinity buffer materials for both types of absorbers. At low temperatures, CBGSe films show free-exciton photoluminescence, as well as pronounced deep-level emission at ~1.4 eV, while CBTS films exhibit a strong bound-exciton signal with noticeably less intense deep-level emission than for CBGSe. Charge carrier kinetics, transport, and recombination properties of both types of films are also analyzed using optical-pump terahertz-probe spectroscopy and time-resolved microwave conductivity. The first CBGSe prototype solar cells (using chemical bath deposited CdS as a buffer layer) show a maximum of 1.5% efficiency with ~0.62 V open-circuit voltage. The measured properties point to possible limiting factors for CBGSe and related films for PV and optoelectronics and provide insights on possible approaches for improvement within this multinary chalcogenide family.

Received 5th July 2021
Accepted 2nd October 2021

DOI: 10.1039/d1ta05666b

rsc.li/materials-a

## Introduction

Kesterite $Cu_2ZnSnS_{4-x}Se_x$ (CZTS), which replaces scarce and expensive group-13 elements indium/gallium in $CuIn_{1-x}Ga_xS_{2-y}Se_y$ (CIGS) with earth-abundant group-12 zinc (Zn) and group-14 tin (Sn), has been considered as an alternative light absorbing material to CIGS for thin-film solar cells. However, the highest power conversion efficiency (PCE) for CZTS devices is only 12.6%, achieved in 2014,[1] far less than the record 23.4% PCE for CIGS analogs.[2] A key limiting factor for CZTS solar cells relates to low open-circuit voltage ($V_{OC}$).[3,4] The $V_{OC}$ deficit in turn correlates, at least in part, with the small energy cost for the exchange between Cu and Zn atoms in the lattice due to their similar size, coordination, and chemical valence.[5–8] The similarities between the two atoms result in formation of a high density of associated anti-site defects and defect-clusters in the CZTS lattice, which may introduce band tailing that can reduce $V_{OC}$ and efficiency of the CZTS solar cells.[9–11] Given the similar sizes and coordination for Cu, Zn and Sn, other permutations of anti-site defects and related defect clusters (*e.g.*, $Cu_{Sn}$, $Zn_{Sn}$, $Sn_{Zn}$, $Cu_{Zn} + Sn_{Zn}$) are expected to contribute to the $V_{OC}$ deficit through band tailing and/or deep defects.[7,12,13]

One possible approach for minimizing anti-site related lattice disorder involves substituting Zn with larger and chemically more differentiated group-2 elements. This approach has introduced a new class of chalcogenides, $I_2$–II–IV–$X_4$ (I = Cu, Ag;

[a]Department of Mechanical Engineering and Materials Science, Duke University, Durham, North Carolina 27708, USA. E-mail: david.mitzi@duke.edu

[b]Department Structure and Dynamics of Energy Materials, Helmholtz-Zentrum Berlin für Materialien und Energie GmbH, Hahn-Meitner-Platz 1, 14109, Berlin, Germany

[c]Department of Physics, Dalhousie University, 6310 Coburg Road, Halifax, Nova Scotia, B3H 4R2, Canada

[d]IBM T. J. Watson Research Center, Yorktown Heights, New York 10598, USA

[e]Department of Chemistry, Duke University, Durham, North Carolina 27708, USA

† Electronic supplementary information (ESI) available. See DOI: 10.1039/d1ta05666b

II = Sr, Ba; IV = Ge, Sn; X = S, Se).[14,15] Sr and Ba not only have larger ionic sizes than Cu, but also have a distinct coordination environment in the $I_2$–II–IV–$X_4$ lattice compared to Zn, which in turn has similar coordination to the I (and IV) atoms.[14] Such dissimilarities between I (and IV) and II elements in $I_2$–II–IV–$X_4$ result in a higher formation energy for related anti-site defects, thus inhibiting formation of severe band tailing.[16–18] Among these compounds, $Cu_2BaSnS_4$ (CBTS) adopts a trigonal ($P3_1$) crystal structure and has a quasi-direct band gap of 2.02 eV.[17] The band gap of CBTS can be reduced to 1.55 eV by partially substituting S with Se to form $Cu_2BaSnS_{4-x}Se_x$ (CBTSSe; $x$ = 3).[17] CBTS and CBTSSe consist of earth-abundant, lower toxicity metals, a favorable situation in terms of prospective production scalability. These properties of CBTS motivate studies related to thin-film synthesis using both solution-[19] and vacuum-based techniques,[16,17,20] as well as their photovoltaic (PV) and water electrolysis applications.[16,19–22] So far, the highest solar cell PCE achieved based on CBTSSe is 5.2% from solar cells based on films prepared by sulfo-selenization of co-sputtered precursor layers.[16]

As of yet, no reports have appeared on films and solar cells based on the related $Cu_2BaGeSe_4$ (CBGSe) system, which is isostructural to CBTS.[14,23] According to Wessler *et al.*,[24] the band gap of CBGSe can be tuned from 1.91 eV to 1.57 eV by partial substitution of Ge with Sn ($Cu_2BaGe_{1-x}Sn_xSe_4$ or CBGTSe). The tunable properties and appropriate range of band gaps show the potential of applying this compound to a light absorbing layer in solar cells. Interestingly, CBTS and CBGSe offer similar band gaps (close to 2 eV).[17,24] However, while CBTS comprises $Cu^+$ and $Sn^{4+}$ ions with similar ionic size, for CBGSe, ionic sizes for $Cu^+$ and $Ge^{4+}$ are distinct (*i.e.*, all metal ions in the CBGSe structure offer substantially distinct ionic radii). It is therefore interesting to consider whether this distinction between CBTS and CBGSe can yield dissimilar defect and electrical transport properties and therefore different prospects for solar-related devices. Another important aspect for efficient solar cells relates to band alignment among device layers. It is known that formation of cliff-type conduction band offset (CBO < 0 eV) between absorber and buffer layer of a solar cell increases the degree of interface recombination, which is detrimental for performance.[25] Band positions of CBTS, with respect to vacuum-level or CdS, have been previously investigated from work function and flat-band potential determination using X-ray photoelectron spectroscopy (XPS) and/or electrochemical Mott–Schottky analysis.[20,26] These studies show that CBTS forms a large cliff-type CBO with a CdS buffer layer, and therefore associated devices are vulnerable to interface recombination. However, the band positions for CBGSe have not yet been reported.

In this study, we prepared CBGSe and analogous CBTS films from selenization or sulfurization of Cu–Ba–Ge and Cu–Ba–Sn precursor layers, deposited sequentially using vacuum-based techniques. The CBGSe and CBTS films were then used for detailed characterization and as a light absorber for solar cells. To identify the key underlying differences between these two compounds, we investigated electronic properties of the CBGSe and CBTS films. Hall effect was used to determine the majority carrier types, concentrations, and mobilities for the semiconductor films. The densities of states near the conduction band and valence band edges have been examined by ultraviolet photoelectron spectroscopy (UPS) and inverse photoemission spectroscopy (IPES) to determine the band positions (*i.e.*, electron affinity and ionization energy). The exciton and defect properties of the films were analyzed with temperature-dependent photoluminescence (PL) measurements. Charge carrier kinetics, transport, and recombination properties of the films were examined with optical-pump terahertz-probe spectroscopy (OPTP) and open-cell time-resolved microwave conductivity (oc-TRMC). The properties of the first prototype CBGSe solar cells were characterized by current density–voltage ($J$–$V$) and external quantum efficiency (EQE). The measured properties reveal possible limiting factors and challenges for PV application of this material, and provide insights on possible approaches for improving the properties of films and analogous PV devices based on this system and related $Cu_2$–II–IV–$X_4$ chalcogenides.

## Experimental section

### Film and device fabrication

CBGSe and CBTS films for PL, optical absorption, and Hall effect measurement were prepared on quartz glass substrates. The deposition process for both types of films consists of three steps: deposition, pre-annealing, and reaction with sulfur/selenium. First, Cu–Ba–Ge and Cu–Ba–Sn precursor layers were deposited by consecutive deposition of multiple stacked layers of Cu, Ge, Sn and Ba using a deposition system (AJA International) equipped with a vacuum chamber, sputter guns and an evaporator. The base pressure of the vacuum chamber was maintained at $<5.0 \times 10^{-7}$ torr. Cu, Ge and Sn layers were deposited by RF sputtering of Cu (99.999%, 3 inch; Kurt J. Lesker), Ge (99.999%, 3 inch; AJA International) and Sn (99.999%, 3 inch; AJA International) targets at 62 W, 60 W and 50 W power, respectively, under 3 mTorr of Ar atmosphere. The Ba layer was deposited by thermal evaporation of Ba pieces (99.7%; Strem Chemicals) under vacuum. The precursor layer configuration is shown in detail in the ESI (Fig. S1†). The substrates were not intentionally heated during the deposition processes. After completing deposition, the metal precursor layers were pre-annealed at 580 °C for 30 min in the same vacuum chamber. This high temperature pre-annealing step was critical for getting uniform CBGSe and CBTS films without blistering, which typically appears for films from sequentially deposited precursor layers.[27] After cooling to room temperature, the substrates were directly transferred into a $N_2$-filled glove box to avoid exposure to ambient air. Then, the substrates were placed on a hotplate at 580 °C for 25 min under Se or S vapor with a quartz cover, for a chemical reaction to convert the metal precursor layers into CBGSe or CBTS films. The experimental setup for the reaction step is described in detail elsewhere.[19] The metal elemental ratios in the final films were in the ranges of Cu/(Ba + Ge) = 0.89–0.92 and Ba/Ge = 1.16–1.22 for CBGSe films and Cu/(Ba + Sn) = 0.87–0.89 and Ba/Sn = 1.03–1.11 for CBTS films, as determined by energy-dispersive X-ray spectroscopy. The Hall bars (Fig. S2†) were patterned by mechanical

 

scribing and selected removal of the films on the substrates. The electrodes for the Hall bars were Ti (10 nm) and Au (100 nm), deposited sequentially through shadow masks by e-beam evaporation.

The films for UPS/IPES measurements and for solar cells were deposited on Mo-coated soda-lime glass substrates and prepared using the same deposition methods as described above, but with a lower pre-annealing temperature of 520 °C. The reaction (selenization/sulfurization) temperature was also relatively low, 500 °C, for both CBGSe and CBTS, in order to control $MoS_2$ and $MoSe_2$ formation at the absorber/Mo interface. CBGSe (and CBTS) solar cells were completed by deposition of a 50 nm-thick CdS buffer layer using the chemical bath deposition (CBD) method at 70 °C followed by sequential deposition of i-ZnO (50 nm) and ITO (150 nm) window layers by RF sputtering.[28–30] Sheet resistance of the ITO layer was ~25 Ω $\square^{-1}$. Ni (45 nm) and Al (700 nm) front electrodes were deposited through shadow masks using e-beam evaporation. The solar cells were then mechanically scribed to define the total device area of ~0.425 $cm^2$. Post-annealing treatment was also conducted on the solar cells to improve the device performance, by placing the devices on a hotplate (at 200 °C) under ambient air for varying amounts of time.

### Characterizations of films and devices

X-ray diffraction (XRD) patterns of the films were acquired at room temperature using a Malvern Panalytical Empyrean diffractometer with Cu Kα radiation ($\lambda = 1.54056$ Å). Scanning electron microscope (SEM) images were acquired using an FEI Apreo S system. Atomic metal compositions of the films were determined by energy dispersive X-ray measurement performed at 30 kV acceleration voltage using the SEM system. Room-temperature PL spectra of the samples were acquired utilizing a Horiba Jobin Yvon LabRam ARAMIS spectrometer, which consists of a microscope, monochromator (focal length 450 mm) and an air-cooled CCD detector. An excitation wavelength of 442 nm from a HeCd laser was chosen for the measurements. Temperature dependent PL was excited with a 409 nm diode laser and analyzed by a 1/2 m grating monochrometer, using a thermoelectrically-cooled Si-CCD and a liquid-nitrogen-cooled InGaAs detector. Samples were mounted on a cold-finger in a helium closed-cycle cryostat. Optical transmittances of the samples were measured using a Shimadzu UV-3600 spectrophotometer. Optical reflectance measurements were acquired with an Enlitech QE-R equipped with integrating sphere.

Hall effect measurement was conducted using a parallel dipole line system that generates a unidirectional and pure single harmonic ac magnetic field,[31] with a magnetic field amplitude of 0.65 T in the plane of the Hall bar. A Keithley 2400 Source Meter Unit (SMU) was used as the current source and a Keithley 2001 Digital Multi Meter (DMM) was employed for voltage measurement. A Keithley 7065 Hall switch matrix card with high impedance buffer amplifiers was used for routing the signals between the samples, the SMU and DMM. The analysis of the Hall signal was performed using custom-developed software created in Matlab.[32] The Hall scattering factor, which generally varies between 1 and 2, is assumed to be $r = 1$ in the current study.[33] This assumption can lead to an error in computed Hall carrier densities and mobilities of up to a factor of two. Additional information on the Hall setup and data analysis can be found elsewhere.[31,33]

*J–V* curves for the CBGSe solar cells under AM1.5G illumination were measured using a customized system consisting of Newport-Oriel Sol2A solar simulator and Keithley 2401 sourcemeter. EQE curves of the solar cells were measured with an Enlitech QE-R equipped with a 75 W Xe light source, monochromator (focal length < 120 mm), two digital signal processing lock-in amplifiers, and an optical chopper (ac probe-light frequency of 165 Hz). Both *J–V* and EQE measurements were calibrated with a reference Si solar cell.

Photoelectron spectroscopy (PES) measurements were performed in an ultra-high vacuum chamber (base pressure of $10^{-10}$ mbar) equipped with X-ray photoelectron spectroscopy (XPS), ultraviolet photoelectron spectroscopy (UPS) and inverse photoelectron spectroscopy (IPES). For XPS and UPS, the analysis chamber was fitted with a Specs Phoibos 150 hemispherical energy analyzer. The initial CBTS XPS spectra were collected using an unmonochromated Al Kα (1486.6 eV) source but, due to a system upgrade, the CBGSe XPS data were collected using a monochromated Al Kα source. The system upgrade results in the CBGSe core levels having smaller FWHMs due to the improved energy resolution of the source photons. UPS measurements were carried out using a He 1 ($h\nu = 21.22$ eV) source. To measure the onset of photoemission in UPS, a −3 V bias was applied to the samples to overcome the contact potential difference between each sample and the analyzer. IPES measurements were performed using a homemade spectrometer that utilizes a band-pass photon detector consisting of an electron multiplier/KCl photocathode coupled with a $SrF_2$ window. This setup was operated in the isochromat mode. The resolution of the IPES setup is ~0.6 eV, as determined by the width of the Fermi edge for clean polycrystalline silver. An $Ar^+$ ion source was utilized for the removal of surface contaminants. The sputtering was performed using an extractor voltage of 300 V and a beam current of 0.1 μA while rastering over the sample area.

Optical-pump terahertz spectroscopy (OPTP) was based on an amplified Ti:sapphire femtosecond laser with 150 kHz repetition rate. For terahertz generation and detection, ZnTe crystals and a double modulation lock-in were used. The pump beam was the second harmonic with a wavelength of 400 nm at a photon flux of ~$10^{13}$ photons per pulse per $cm^2$. The open cell time-resolved microwave conductivity (oc-TRMC) measurement uses the $K_a$-band at ~30 GHz for microwave generation and the same laser pulses for photoexcitation as the OPTP setup.

## Results and discussion

### Basic film properties

XRD patterns and SEM images of CBGSe and CBTS films prepared on quartz glass substrates are shown in Fig. 1a and b. The XRD patterns of the films match simulated patterns for each material without appearance of any secondary peaks (even when plotting on a log intensity scale), pointing to the single-

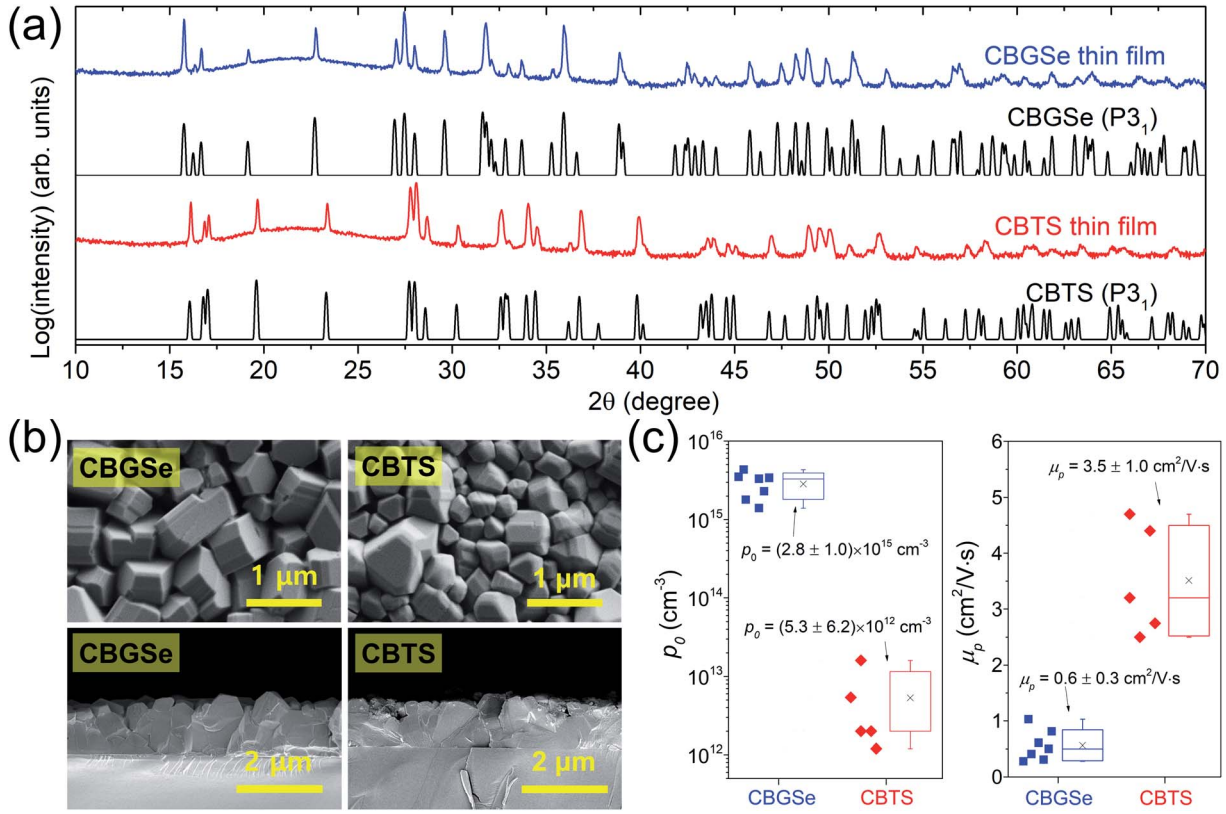


Fig. 1 X-ray diffraction (XRD) patterns of (a) CBGSe (blue line) and CBTS (red line) films deposited on quartz glass substrates. The patterns are compared with simulated XRD patterns (black lines), created using CrystalDiffract software with lattice parameters adapted from ICDD reference codes 01-71-2889 for CBGSe and 03-65-7569 for CBTS. (b) SEM surface and cross-section images. The cross-section images of the films were taken after depositing a thin gold layer (<5 nm) to suppress surface charging. (c) Statistical distribution of the hole carrier densities ($p_0$) and hole mobilities ($\mu_p$) extracted from Hall measurements on several distinct CBGSe and CBTS Hall bars. The boxes are determined by (average) ± (standard deviation), and the "*x*" marks represent the averages and the horizontal lines correspond to the medians. Whiskers represent maximum and minimum data points.

phase nature of both film types. The SEM images indicate overall average film thicknesses of approximately 1.1 μm and 1.0 μm for CBGSe and CBTS, respectively. Despite similar reaction conditions, the CBGSe film grain widths are generally slightly larger on average than for corresponding CBTS films (average grain widths are ~580 nm for CBGSe and ~370 nm for CBTS, as estimated from the square-root of the area divided by the number of grains within each of the surface SEM images). The larger grain size may be due to liquid-assisted grain growth in the $GeSe_2$–Se system, as also reported for $Cu_2Zn(Sn,Ge)Se_4$ films.[34,35] We note that, since quartz glass substrates do not contain sodium, in contrast to soda-lime glass, the films on these substrates are expected to be relatively free of sodium impurities, which are known to impact film morphology and/or recombination properties in CIGS and CZTS systems.[36–38] We expect that the nominally comparable crystal structure, band gap and film morphologies between CBGSe and CBTS films will enable direct comparison of their carrier transport and bulk recombination properties, as well as assessment of their potential as PV materials. XRD patterns and SEM images of CBGSe and CBTS films deposited on Mo-coated soda-lime glass substrates are shown in Fig. S3.† The XRD patterns confirm that both films predominantly consist of the targeted CBGSe and CBTS phases (although the CBTS film shows small diffraction peaks that likely correspond to a barium sulfide phase).

Hall measurements were performed on CBGSe and CBTS Hall bars to determine the carrier type (p- or n-), density and mobility. Examples of Hall coefficient extraction are given for both CBGSe and CBTS in ESI (Fig. S4 and S5†). Both CBGSe and CBTS films offer p-type semiconducting behavior. CBGSe exhibits a sample-averaged hole carrier density of $p_0 = (2.8 \pm 1.0) \times 10^{15}$ cm$^{-3}$, which is three orders of magnitude higher than the analogous density of $p_0 = (5.3 \pm 6.2) \times 10^{12}$ cm$^{-3}$ for CBTS (Fig. 1c). We note that, in the case of CBTS, acceptor-like $V_{Cu}$ is expected to be the dominant defect,[18] contributing to p-type conductivity. The noticeably higher hole carrier density of CBGSe compared to CBTS may imply shallower (or higher density of) $V_{Cu}$ or a smaller concentration of compensating donor defects in CBGSe. A hole mobility of $\mu_p = 0.6 \pm 0.3$ cm$^2$ V$^{-1}$ s$^{-1}$ is measured for CBGSe, while CBTS shows higher hole mobility of $\mu_p = 3.5 \pm 1.0$ cm$^2$ V$^{-1}$ s$^{-1}$.

## Photoelectron spectroscopy

To examine band positions of CBGSe and CBTS with respect to the vacuum level, we have conducted UPS/IPES measurements.

 

UPS/IPES spectra of CBGSe and CBTS films with different mild Ar ion (0.3 keV) sputtering time are illustrated in Fig. 2. For the CBTS film, the near-band-edge and onset region spectra show a convergence after 80 min of mild sputter etching, implying that impurities at the CBTS film surface have been effectively removed, exposing nominally intrinsic material properties. That impurities are being removed is confirmed by the reduction in UPS signal in the 6 eV–12 eV range, typically attributed to states resulting from the hybridization of the low-lying O 2p core level, as well as the XPS close-up scans of the carbon and oxygen surface contaminants (Fig. S6†). For the CBGSe film, convergence is slower, but the cut-off and onset region values approach convergence after 120 min of sputtering. We note that XPS spectra of both CBGSe and CBTS films do not show significant changes in the line-shapes, relative intensities, and binding energies of Cu 2p, Ba 3d, Ge 3d, Sn 3d, S 2p and Se 3d core-levels with increasing $Ar^+$ exposure times (with the possible exception of Cu, which will be discussed later) after removal of surface contaminants (Fig. S6 and S7†), indicating that the sputter cleaning does not introduce severe compositional changes of the clean material surfaces (Tables S1 and S2†).

Fig. 3 summarizes measured valence band maximum (VBM) and conduction band minimum (CBM) positions determined by UPS and IPES, respectively, along with calculated electron affinity (EA) and band gap ($E_g$) values for CBGSe and CBTS films. The parameters derived at different low-energy sputtering times are summarized in Table S3.† Once the samples are sputtered for long enough times to sufficiently remove nearly all surface contamination, the estimated $E_g$ values from UPS/IPES of ~1.9 ± 0.2 eV and ~2.0 ± 0.2 eV for CBGSe and CBTS, respectively, agree well with the band gaps determined from optical absorption spectra (see discussion below). The electron affinity values are measured to be 3.72 ± 0.2 eV and 3.28 ± 0.2 eV for CBGSe and CBTS, respectively. We also note that CdS, which is a material that has been widely used as a reference buffer layer in thin film solar cells, offers an electron affinity of 4.15 ± 0.3 eV from our previous UPS analysis.[39] Thus, both CBGSe and CBTS compounds are expected to form a large cliff-type CBO with a CdS buffer layer. In the Schottky limit, where the CBO of a junction equals the difference in electron affinity values for the two contacting materials, the CBGSe/CdS junction will have a cliff-type CBO of approximately −0.43 eV, while the CBTS/CdS junction will have an even larger cliff-type CBO corresponding to −0.87 eV. Large negative CBOs are expected to reduce the effective distance between the conduction band maximum of CdS and valence band minimum of CBGSe (or CBTS) at the interface and promote recombination of charge carriers.[25] We note that, in a previous study,[26] CBTS electron affinity was

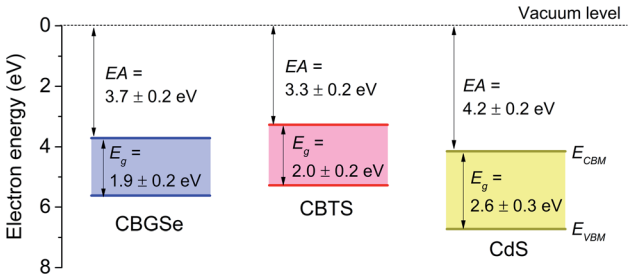


Fig. 3 Energetic positions of conduction band minimum ($E_{CBM}$) and valence band maximum ($E_{VBM}$) for CBGSe, CBTS and CdS determined from UPS/IPES measurements. The data for CdS is from ref. 39.

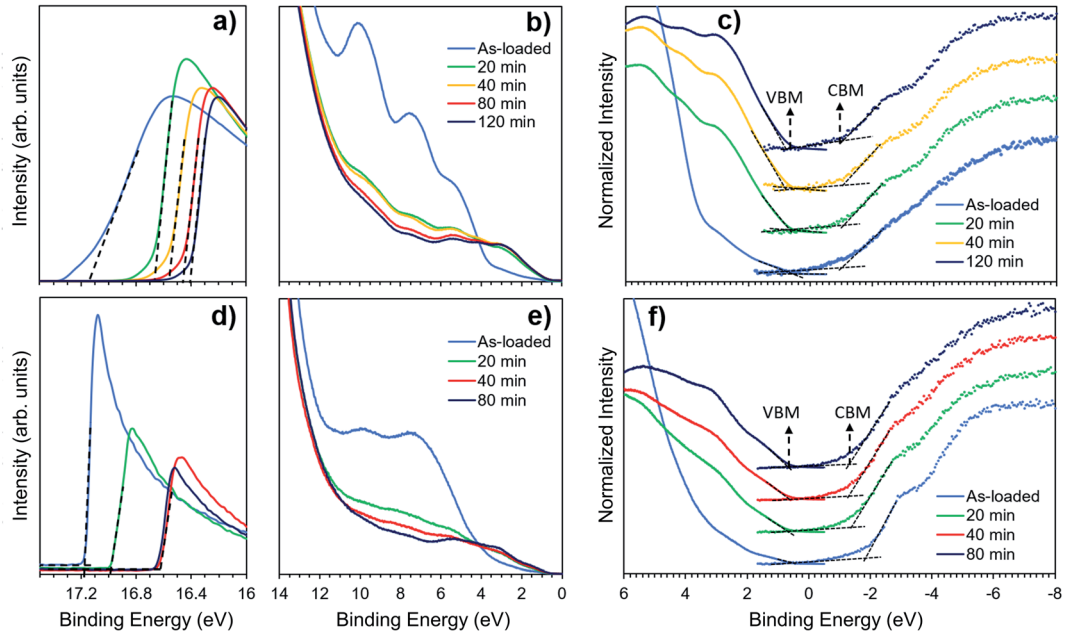


Fig. 2 UPS and IPES spectra for (a–c) CBGSe and (d–f) CBTS films with varied $Ar^+$ sputtering times (300 V), including (a and d) UPS He 1 secondary electron onset, (b and e) scans of valence band states and (c and f) combined close-ups of UPS He 1 valence band edge and IPES conduction band edge (filled circles).Tangent lines are drawn to show intersection with the background to mark the onset in (a and d). $E_{VBM}$ and $E_{CBM}$ are marked by dashed lines in (c and f).

estimated from XPS and electrochemical Mott–Schottky analysis to be 3.67 eV. Even though the electron affinity determined by these authors is larger than the value derived in our current study (~3.3 eV from UPS/IPES analysis), both values suggest that CBTS would form a large negative CBO with CdS, which would serve to limit the device performance.

In addition, XPS depth profiling of the surface region by Ar etching shows that CBTS has a Cu-poor surface (Table S1†), while CBGSe has a Cu-poor/Ba-rich surface (Table S2†). For CBTS, it is possible that this surface region might contain a very thin secondary phase such as $Cu_2Ba_3Sn_2S_8$, which forms during CBTS synthesis under S deficient and high temperature conditions.[40] This phase is known to have slightly larger band gap (2.19 eV) than CBTS.[40] Similarly, CIGS films have been reported to exhibit Cu-deficiency on the surface,[41] which enhances diffusion of Cd into the films,[41,42] resulting in carrier type inversion of the CIGS film surfaces and formation of a buried junction.[43] Metal stoichiometry variation at the surfaces may at least partially account for the unexpected positions of the Fermi levels relative to $E_{VBM}$ values (Table S3†), which do not agree with bulk carrier densities derived from Hall effect measurements. Detailed impact of surface chemistry on device properties is also currently unknown and requires further investigation.

## Optical spectroscopy

Next, we examine the unique shape of the optical absorption coefficient ($\alpha$) spectra, which exhibit similar onsets at approximately 2 eV (Fig. 4) in both materials. Note that, although we find good general agreement between the absorption coefficient derived from transmission/reflection measurements and from the EQE of the CBGSe and CBTS solar cells (as presented in a later section), we used the latter for the discussion below, because of the presence of scattering artifacts (perhaps associated with film roughness) in the UV-Vis-derived absorption in the long wavelength region. A shoulder and slight peak can be seen for CBTS towards lower photon energies, which has recently been attributed to a free exciton.[26] Modeling the absorption coefficient of CBTS with the Elliott model for exciton absorption (as detailed in ESI Note S1†) yields an $E_g$ of 2.098 ± 0.010 eV and an exciton binding energy of 25 ± 5 meV. A previous report on CBTS estimated significantly larger exciton binding energies of 37 meV from ellipsometry data and 64 meV from transmission measurements.[26] The absorption properties of CBGSe are found to be more complex and may be modeled by contributions from two band edge transitions: a lower transition of 2.03 ± 0.01 eV and a higher transition at 2.10 ± 0.01 eV, as well as an excitonic contribution with a binding energy of 20 ± 5 meV for each transition. The observation of these two distinct band edge transitions indicates the possible presence of a split-off valence band at the Γ point, featuring allowed transitions to the conduction band as has been found in $CuGaSe_2$.[44] Although DFT calculations also indicated the presence of an indirect transition 10 meV below the direct transition,[14] we do not expect this to influence the absorption measurement, due to the much lower transition probability for the indirect band edge.

The static dielectric constant, $\varepsilon_0$, is not experimentally known in these materials, but a slightly lower free-exciton binding energy of CBGSe in comparison to CBTS is expected due to the previously reported smaller computed relative effective masses of electrons $m_e$ (0.16 for CBGSe *vs.* 0.22 for CBTS) and holes $m_h$ (0.41 for CBGSe *vs.* 0.64 for CBTS), which result in exciton reduced masses, $\mu$, of 0.16 (CBTS) and 0.12 (CBGSe),[14,45] calculated as the geometric mean[45] of the corresponding effective mass values along *a*, *b*, and *c* crystallographic directions.[14] From the well-known equation for the exciton ground state, $E_{FX} = Ry \times \mu/{\varepsilon_0}^2$, where Ry = 13.6 eV is the Rydberg energy, we estimate static dielectric constants of 9.3 ± 1.3 and 9.0 ± 1.4 for CBTS and CBGSe, respectively. A lower theoretical value of $\varepsilon_0$ = 6.1 has been calculated previously for CBTS.[46]

To assess the possible effect of excitons on the optoelectronic properties of solar cells, the fraction of free charge carriers over total charge carriers including excitons, also called free carrier quantum yield ($\phi$), has been determined using the Saha equation (see ESI Note S2†).[47,48] The free carrier quantum yield at room temperature is shown in Fig. S8† for a wide range of free carrier densities and the two exciton binding energies of 20 meV and 25 meV. The analysis shows that, for carrier densities

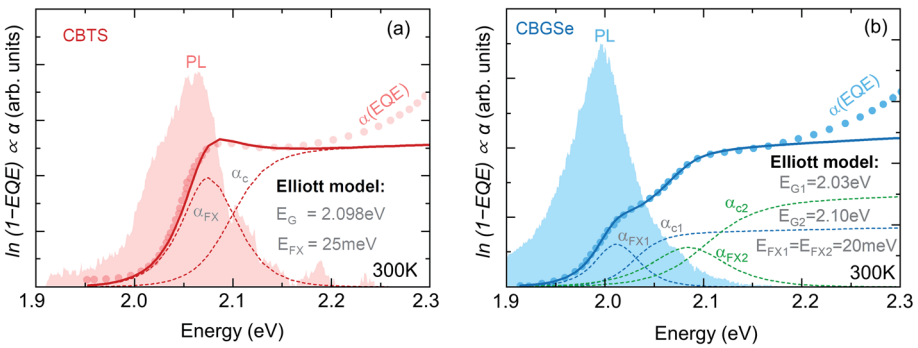


Fig. 4 Room-temperature photoluminescence (PL) and absorption coefficient spectra of the (a) CBTS and (b) CBGSe films. The absorption data are analyzed using the Elliott model, leading to free exciton binding energies of 25 meV (CBTS) and 20 meV (CBGSe). Note, that the GBGSe spectrum is modeled with an additional high energy transition at 2.10 eV and associated exciton contribution with a binding energy of 20 meV.

 

expected under solar cell operation, the free carrier quantum yield at room temperature approaches unity, indicating negligible exciton concentrations under steady state conditions. Thus, no detrimental influence of the excitons on the charge carrier mobility or PV application of the material is expected.

Although the PL emission at room temperature shown in Fig. 4a and b appears to originate from the excitonic region, the estimation of the free-carrier quantum yield discussed in the last paragraph suggests that, at room temperature, the luminescence is dominated by band-to-band transitions, with a minor influence of excitons. The temperature dependence of the PL for CBTS (Fig. 5a) shows that the room temperature PL blueshifts to 2.107 eV and significantly narrows as the temperature decreases to ~50 K. This blueshift agrees with the observations by Crovetto *et al.*, (although their transitions are shifted to lower energy by 30–40 meV),[46] and can be explained with the temperature dependence of the band gap.[20] The significant narrowing of the transition below 100 K indicates that, for low temperatures, the emission from the free exciton is observed. Below 50 K, another sharp line appears 30 meV below the free exciton transition, which dominates over the free exciton at lower temperatures and which we attribute to an exciton bound to a defect in accordance with literature.[26,46] The additional binding energy of the bound exciton is 30 meV, as determined by the energy difference between the respective PL transitions.

For CBGSe, the band edge PL peak also blue shifts with decreasing temperature (Fig. 5b), which in analogy to CBTS can be interpreted as the temperature dependence of the band gap. However, in this case, we only observe the evolution of a free exciton, with no bound excitonic line being observed at cryogenic temperatures. As can be seen in Fig. 5c, both CBGSe and CBTS exhibit PL peaks below the excitonic transitions at low temperature, with transition energies of 2.016 eV and 1.962 eV, respectively. These can be attributed to shallow defect transitions. For CBGSe, these defects are only 90 meV from the band edges and may be related to the acceptors responsible for the doping density measured by the Hall measurement. For the CBTS film, the shallow defects are deeper within the band gap (140 meV), which reduces associated defect ionization and thus the release of free charge carriers, perhaps explaining (or contributing to) the low doping level observed for this material. Additionally, deep luminescence at ~1.4 eV is more pronounced for CBGSe than for CBTS and reflects a similar situation to that reported for CSTS,[26] pointing to CBGSe having a higher concentration of deep-level defects than CBTS (at least for the current film preparation conditions). The PL peaks of CBGSe at 1.4 eV–1.6 eV indicate defects that are approximately 400 meV–700 meV below the band edges. Since deep-levels usually dominate Shockley–Read–Hall recombination, this suggests that CBGSe may suffer from a high degree of nonradiative recombination.

Recombination and charge carrier kinetics were also probed by transient photoconductivity using optical pump terahertz probe spectroscopy (OPTP) and open-cell time-resolved microwave conductivity (oc-TRMC) (Fig. 6). The decay of the photoconductivity measured by OPTP (Fig. 6c) features an initial fast decay of about 10 ps followed by a longer decay time of 0.9 ns and 1.7 ns for CBTS and CBGSe, respectively. The photoconductivity transients from OPTP and oc-TRMC are combined in Fig. 6a, with the differential decay time plotted in Fig. 6b. The differential decay time constant increases from ~3 ps shortly after the excitation pulse, to a value of order 1 ns at intermediate delay times, to beyond a microsecond for further increasing delay times for both CBTS and CBGSe. In the previous OPTP studies on CBTSSe and $Cu_2ZnSnSe_4$, longer decay components were observed after an initial fast decay of photoconductivity, which was attributed to surface recombination.[39,49] We expect that most of the incident excitation light is absorbed near the surface of CBGSe and CBTS films, considering the very short penetration depth (~39 nm for CBGSe and ~44 nm for CBTS) of light with 400 nm wavelength for both CBGSe and CBTS, estimated from the inverse of the optical absorption coefficients (Fig. S9†). To more definitively clarify the influence of surface recombination in the current samples, an additional excitation source with a wavelength of 400 nm < $\lambda$ < 620 nm would be

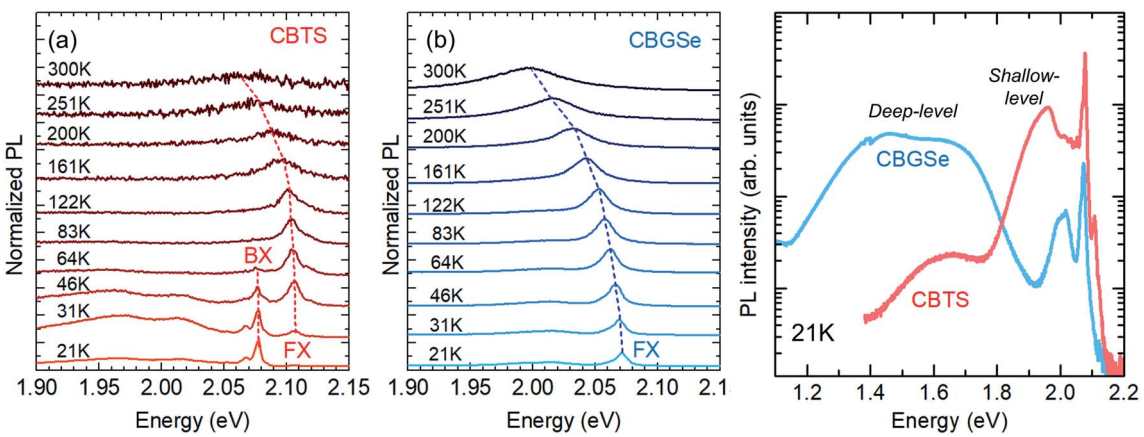


Fig. 5 Temperature-dependent PL spectra showing: (a) excitonic region for CBTS with free exciton (FX) and bound exciton (BX). (b) Excitonic region for CBGSe with free exciton (FX). (c) Comparison of PL from deep-level defects at 21 K (note logarithmic PL intensity scale).

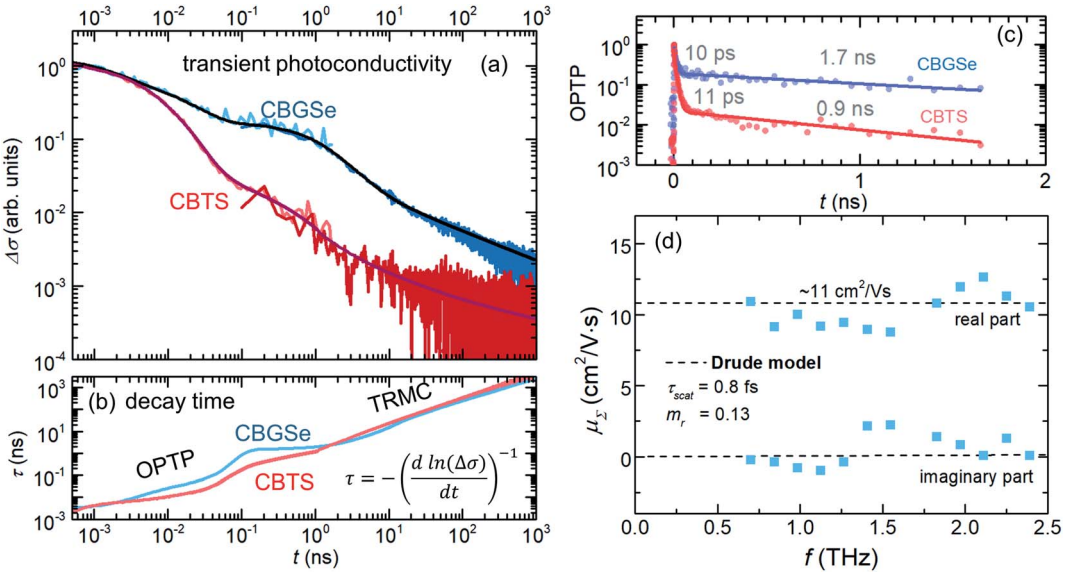


Fig. 6 Transient behavior for CBTS and CBGSe. (a) Photoconductivity transients measured by optical-pump terahertz-probe spectroscopy (OPTP) (100 fs–1.8 ns) and by open-cell time-resolved microwave conductivity (oc-TRMC) (100 ps–1 μs) on CBGSe and CBTS films. The solid lines are guides to the eye. (b) Differential decay time of CBGSe and CBTS films derived from the transient photoconductivity. (c) Photoconductivity transients measured by OPTP. (d) Sum of electron and hole mobilities at terahertz frequencies, $\mu_\Sigma$, measured by OPTP and modeled by the Drude model of free charge carrier transport (dashed line) for the CBGSe sample, yields a scattering time, $\tau_{scat}$, of 0.8 fs for a reduced effective mass, $m_r$, of 0.13.

required, which is currently not available in our experimental setup. Still, considering the similarity in materials and processing conditions between CBGSe/CBTS and previously studied lower band gap CBTSSe,[39] the fast initial decay in Fig. 6c for both CBGSe and CBTS may reasonably be attributed to surface recombination. Although this initial fast decay time will dominate the recombination (and therefore solar cell performance) in a device, the larger intermediate decay time on the order of 1 ns may correspond to the true bulk lifetime without influence of the surface. We note that a lifetime of 1–2 ns would be still considered relatively modest compared to lifetimes in state-of-the-art chalcopyrite or perovskite materials, which can reach several hundred nanoseconds to microseconds. The origin of the long decay times at large delays is not immediately clear, but could be due to detrapping from deep-levels, which become filled at the beginning of the transient. Such detrapping can produce apparent decay times that greatly exceed the true minority carrier lifetimes, dependent on the energy depths of the trapping levels.[50] We note that, for both CBTS and CBGSe, deep trap levels have been detected in the low temperature PL measurements (Fig. 5c), thus providing support for this interpretation.

The terahertz mobility of CBGSe was measured by OPTP at 200 ps after photoexcitation and scaled to the initial amplitude of the photoconductivity transient. In the measurement, the sum of electron and hole mobility, $\mu_\Sigma$, is probed at very high alternating currents that oscillate at terahertz frequencies (Fig. 6d). The real and imaginary parts exhibit a rather flat frequency-dependence for CBGSe, which indicates free charge carrier transport with short scattering times. The short scattering time may indicate the presence of high density of scattering sites – *e.g.*, ionized defects in CBGSe. Fitting the spectra with the Drude model (ESI Note S3†), yields an extremely short scattering time of only 0.8 fs, if a reduced relative effective mass ($m_r$) of 0.13 is assumed, in accordance with DFT calculations.[14] Assuming equal scattering times for electrons and holes and effective masses of 0.16 and 0.65,[14] the sum mobility of 11 $cm^2\ V^{-1}\ s^{-1}$ can be separated into hole mobility of 2.2 $cm^2\ V^{-1}\ s^{-1}$ and electron mobility of 8.8 $cm^2\ V^{-1}\ s^{-1}$. The lower Hall-derived hole mobility of $0.6 \pm 0.3$ $cm^2\ V^{-1}\ s^{-1}$ can be explained by transport barriers at grain boundaries, which do not affect the OPTP derived terahertz mobility.[51] We also note that for CBTS we obtain an averaged sum mobility of approximately 24 $cm^2\ V^{-1}\ s^{-1}$, which is of similar order as the value for CBGSe, while both values are significantly lower than the 140 $cm^2\ V^{-1}\ s^{-1}$ previously observed for the related material, CBTSSe.[39]

## CBGSe prototype solar cells

To provide a first indication of the PV potential of the CBGSe system, we fabricated and evaluated (Fig. 7) CBGSe prototype solar cells with a structure based on CBD-CdS as buffer and sputter-deposited i-ZnO and ITO as window layers (see cross-section SEM image in Fig. S10,† which also indicates a CBGSe film thickness of ~1.0–1.2 μm). The impact of post-annealing treatment (at 200 °C) on the devices under ambient air was also considered (similar to a previous CBTSSe study[16]). After initial 5 min of post-annealing, $V_{OC}$, $J_{SC}$, and PCE values for the 12 devices considered show a drastic increase while FF values decrease (Fig. 7a). Extending annealing treatment to 20 min did not cause noticeable changes in overall solar cell parameters. *J–V* curves for one of the highest-performing solar cells (Fig. 7b) yielded the following improvement after the 20 min anneal:

 

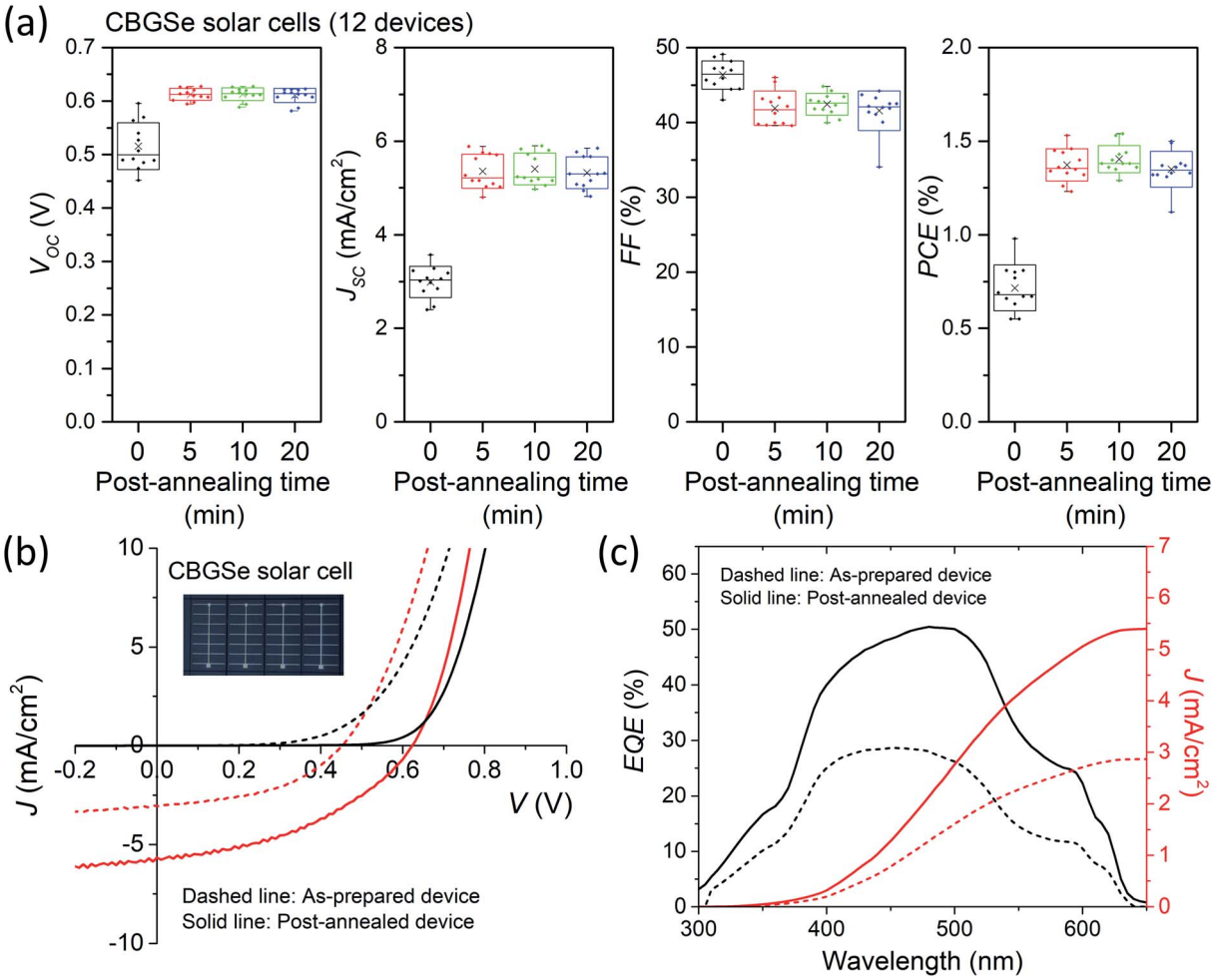


Fig. 7 (a) Statistical distribution of the solar cell performance parameters of 12 prototype CBGSe solar cells with ITO/i-ZnO/CdS/CBGSe/Mo/soda-lime glass structure. The change in the parameters with increasing post-annealing treatment time (at 200 °C under ambient air) is also shown. The boxes are determined by (average) ± (standard deviation), and the "*x*" marks represent the average values and the horizontal lines correspond to the medians. Whiskers represent maximum and minimum data points. (b) *J*–*V* and (c) EQE (with integrated photocurrent densities on the right axis) curves of a representative CBGSe solar cell (before and after post-annealing at 200 °C for a total of 20 min). Inset: an optical image of four CBGSe solar cell devices, each with device area of 0.425 cm$^2$. Black and red lines in (b) represent dark and light *J*–*V* curves, respectively.

452 mV → 623 mV $V_{OC}$, 3.08 mA cm$^{-2}$ → 5.67 mA cm$^{-2}$ $J_{SC}$, 45.2% → 42.5% FF, and 0.63% → 1.50% PCE. The maximum PCE of a post-annealed CBGSe device is comparable to that reported for co-sputtered CBTS solar cells with CBD-CdS as a buffer layer (PCE = 1.6%), with however a lower $V_{OC}$ value (*i.e.*, $V_{OC}$ ≈ 713 mV for the co-sputtered CBTS device).[17] For comparison, an analogous as-prepared CBTS solar cell with the same structure as the current CBGSe device (*i.e.*, CBD-CdS as buffer and sputter-deposited i-ZnO and ITO as window layers) and fabricated using the same approach as the CBGSe devices, yielded a PCE of 1.31% (see Table 1). While $J_{SC}$ of the current CBTS devices show similar improvement to the CBGSe devices after post-annealing (Fig. S11†), $V_{OC}$ and FF decrease significantly with increasing post-annealing time, leading to only small changes in overall PCE.

One-diode device parameters, including reverse saturation current ($J_0$), ideality factor ($n$), series resistance ($R_S$), and shunt conductance ($G_{Sh}$), are derived from *J*–*V* data associated with a representative CBGSe device using the Lambert-*W* function fitting method (Table 1).[52] According to this fitting (Fig. S12†), the as-prepared CBGSe device is limited by high $J_0$, $n$ (>1), $G_{Sh}$, and $R_S$. Post-annealing treatment partly reduces these parameters ($J_0$, $n$, and $R_S$), except for $G_{Sh}$, which shows a noticeable increase (0.7 mS cm$^{-2}$ → 3.9 mS cm$^{-2}$). Among these, high $J_0$ (>1 × 10$^{-3}$ mA cm$^{-2}$) indicates a high degree of recombination loss, which in turn limits solar cell $V_{OC}$. High $n$ (>1) value suggests that the dominant recombination path might be associated with the space charge region (although further more detailed device measurements must be conducted to confirm this assignment).[53] The CBGSe solar cell shows high $R_S$ (3.1 Ω cm$^2$; Table 1). In this case, contribution from bulk CBGSe to $R_S$ (*i.e.*, $R_{S,CBGSe}$) is expected to be ~0.7 Ω cm$^2$, estimated using the Hall data and the following equation: $R_{S,CBGSe} = t/p_0 e\mu_p$, where $t$ is the CBGSe film thickness. Optimization in the CBGSe film thickness and sheet

Table 1 Solar cell performance parameters, and one-diode model parameters from light $J$–$V$ curves derived using the Lambert-$W$ function fitting method[52] from a representative as-deposited and post-annealed CBGSe and CBTS solar cell

| | $V_{OC}$ (mV) | $J_{SC}$ (mA cm$^{-2}$) | FF (%) | PCE (%) | $J_0$ (mA cm$^{-2}$) | $n$ | $R_S$ (Ω cm$^2$) | $G_{Sh}$ (mS cm$^{-2}$) |
|---|---|---|---|---|---|---|---|---|
| As-prepared CBGSe device | 452 | 3.08 | 45.2 | 0.63 | $5.6 \times 10^{-2}$ | 4.5 | 3.6 | 0.7 |
| Post-annealed (200 °C/20 min) CBGSe device | 623 | 5.67 | 42.5 | 1.50 | $1.3 \times 10^{-3}$ | 3.1 | 3.1 | 3.9 |
| As-prepared CBTS device | 758 | 3.04 | 56.7 | 1.31 | $2.0 \times 10^{-6}$ | 2.1 | 4.7 | 1.1 |
| Post-annealed (200 °C/24 min) CBTS device | 633 | 4.64 | 47.4 | 1.39 | $3.1 \times 10^{-4}$ | 2.7 | 9.2 | 2.6 |

resistances of the ITO and Mo/$MoSe_2$ layers may improve the $R_S$ and FF values. Finally, the significant enhancement of $G_{Sh}$ values upon annealing, which also adversely impacts FF, may arise due to reduction in contact resistances among the device layers (expected to be particularly impactful where there are pinholes). Because the post-annealing temperature (200 °C) is noticeably lower than the formation temperature (~500 °C) for the absorber layer, it is not expected that the pinhole densities change for the CBGSe films during the annealing process.

The low EQE values (<30% in the as-deposited device; see Fig. 7c) at short wavelength (400 nm–500 nm) reflect both optical losses within the CdS layer due to its band gap value, which corresponds to 520 nm wavelength,[54] and carrier collection losses from the near-heterojunction region of the absorber layer. The device also shows even lower response (EQE < 20%) in the long wavelength region (>500 nm), likely reflecting low carrier collection efficiency in the bulk region of the absorber layer associated with a high density of recombination centers.[55] As shown in Fig. 7c, the EQE values of the post-annealed CBGSe devices show marked improvement, perhaps through passivation of defects or grain boundaries. Defect passivation by post-annealing has also been demonstrated and is known to be beneficial for CZTS devices, due in part to oxide ($SnO_x$) formation at the grain boundaries and interfaces, which provides a type-I band offset with CZTS at these boundaries, thereby suppressing recombination of charge carriers.[56] However, even after post-annealing treatment, the relatively limited EQE values for the CBGSe solar cell as compared to devices based on other materials such as CBTSSe (whose EQE at $\lambda >$ 500 nm wavelength reaches well above 60%),[16] indicate limited charge carrier collection in the CBGSe device, presumably due to significant interface/bulk recombination, which may also be responsible for the observed large $V_{OC}$ deficit ($=E_g/q - V_{OC} = \sim$1.3 V) for the CBGSe solar cells.

## Conclusions

CBGSe and CBTS compounds share important similarities in terms of high-level properties – *i.e.*, they have the same trigonal crystal structure ($P3_1$ space group) and similar quasi-direct band gaps (~2.0 eV). To identify the key differences and similarities in the underlying properties between these two compounds, electronic characteristics (*i.e.*, electron affinity, hole carrier concentration and mobility, defect levels, recombination, and charge carrier kinetics) have been examined for associated vacuum-deposited thin films employing various techniques (*i.e.*, Hall effect, UPS/IPES, temperature-dependent PL, OPTP, and oc-TRMC). The optical absorption characteristics of CBGSe and CBTS films were modeled using the Elliott equation for exciton absorption, yielding room temperature band gap values of 2.03 ± 0.01 eV and 2.098 ± 0.010 eV and estimated exciton binding energies of 20 meV and 25 meV, respectively. According to the free carrier quantum yield ($\phi$), estimated using the Saha equation and derived exciton binding energies, negligible exciton concentrations under steady state conditions at ambient temperatures would be expected for both CBGSe and CBTS films, pointing to no detrimental effect from excitons within associated solar cells. The room-temperature PL spectra for both types of films therefore also predominantly originate from band-edge emission, while at low temperature free (for both CBGSe and CBTS) and bound (for CBTS) excitons become important. At low temperature, deep luminescence (~1.4 eV from the band-edge) is considerably more pronounced for CBGSe than for CBTS, suggesting the presence of a broader and/or higher concentration of deep-level defects in CBGSe. These defects (potential recombination centers) may lead to a higher degree of nonradiative recombination in CBGSe than for analogous CBTS films, and point to a need to develop defect passivation strategies for this absorber.

Recombination and charge carrier kinetics of CBGSe and CBTS have also been examined from photoconductivity transients measured by OPTP and oc-TRMC. For both systems, we observe a fast decay followed by a slow decay component. The fast decay (~10 ps time constant) dominates the initial recombination of charge carriers for both CBGSe and CBTS films. Because most of the incident light excitation (400 nm wavelength) is absorbed near the film surface (<50 nm depth), the fast initial decay in photoconductivity may arise due to surface recombination. UPS/IPES-derived electron affinity values of approximately 3.7 eV and 3.3 eV for CBGSe and CBTS films, respectively, point to large cliff-type CBOs with a CdS buffer layer (EA = 4.15 eV),[39] which may therefore worsen interface recombination losses in prospective PV devices. According to the Hall measurements, CBGSe exhibits a higher bulk hole carrier concentration (~$3 \times 10^{15}$ cm$^{-3}$) compared to CBTS (~$5 \times 10^{12}$ cm$^{-3}$), possibly due to shallow defect levels (*e.g.*, $V_{Cu}$ defects[18]) being relatively closer to the band edge in CBGSe (90 meV) compared to CBTS (140 meV), according to associated low-temperature PL spectra. The Hall measurements also reveal low hole mobility of ~0.6 cm$^2$ V$^{-1}$ s$^{-1}$ for CBGSe relative to CBTS (~3.5 cm$^2$ V$^{-1}$ s$^{-1}$). The difference between the CBGSe Hall-derived hole mobility (~0.6 cm$^2$ V$^{-1}$ s$^{-1}$) and inferred OPTP-derived value (~2.2 cm$^2$ V$^{-1}$ s$^{-1}$) may reflect transport barriers at

 

grain boundaries for the former measurement. The OPTP-derived terahertz electron/hole sum mobility values are relatively low for both CBGSe (~11 $cm^2 V^{-1} s^{-1}$) and CBTS (~24 $cm^2 V^{-1} s^{-1}$) films compared to the value previously measured for the related CBTSSe material (140 $cm^2 V^{-1} s^{-1}$),[39] suggesting the presence of a higher density of scattering sites (*e.g.*, ionized defects).

We also report the first prototype CBGSe solar cells based on a baseline structure typically used for multinary chalcogenide solar cells (*i.e.*, using a CdS/i-ZnO/ITO top stack). As-prepared CBGSe solar cells yield a relatively limited $V_{OC}$ (~0.45 V) compared to analogously prepared CBTS devices (~0.76 V). The CBGSe devices show noticeable improvement after a post-annealing treatment (at 200 °C for up to 20 min in air), and yield a maximum PCE of ~1.5% with $V_{OC}$ of 0.62 V. However, even after the treatment, the device still shows large $V_{OC}$ deficit (~1.3 V) and limited quantum efficiency (<60%), which likely reflects a large performance loss due to bulk and interface recombination. The combination of substantial sub-band gap luminescence (mentioned above) combined with evidence for surface recombination points to the need for developing defect and interface passivation strategies for improving the solar cell performance. Furthermore, the low electron affinity (~3.7 eV) for CBGSe necessitates pursuing low electron affinity buffer materials, such as ZnS, ZnSe and $Ga_2O_3$, to minimize the interface recombination. Finally, the band gap for CBGSe ($E_g \approx$ 2 eV) can be appropriate for a top cell of a tandem device, while it is too large for high efficiency single heterojunction solar cells, according to Shockley–Queisser considerations.[57] The limited carrier collection of CBGSe in a single-junction solar cell can likely be improved by adjusting the band gap – *e.g.*, by partial substitution of Ge with Sn to achieve a more optimum value, *i.e.*, 1.0 eV < $E_g$ < 1.6 eV.[24]

## Conflicts of interest

There are no conflicts to declare.

## Acknowledgements

This material is based upon work supported by the U. S. Department of Energy, Office of Science, Basic Energy Sciences (BES), under contract DE-SC0020061. This work was performed in part at the Duke University Shared Materials Instrumentation Facility (SMIF), a member of the North Carolina Research Triangle Nanotechnology Network (RTNN), which is supported by the National Science Foundation (award number ECCS-2025064) as part of the National Nanotechnology Coordinated Infrastructure (NNCI). All opinions expressed in this paper are the authors' and do not necessarily reflect the policies and views of the U.S. DOE or NSF.

## References

1 W. Wang, M. T. Winkler, O. Gunawan, T. Gokmen, T. K. Todorov, Y. Zhu and D. B. Mitzi, *Adv. Energy Mater.*, 2014, **4**, 1301465.
2 M. Green, E. Dunlop, J. Hohl-Ebinger, M. Yoshita, N. Kopidakis and X. Hao, *Prog. Photovoltaics*, 2021, **29**, 3–15.
3 S. Bourdais, C. Choné, B. Delatouche, A. Jacob, G. Larramona, C. Moisan, A. Lafond, F. Donatini, G. Rey and S. Siebentritt, *Adv. Energy Mater.*, 2016, **6**, 1502276.
4 D. B. Mitzi, O. Gunawan, T. K. Todorov and D. A. R. Barkhouse, *Philos. Trans. R. Soc., A*, 2013, **371**, 20110432.
5 S. Chen, X. Gong, A. Walsh and S.-H. Wei, *Appl. Phys. Lett.*, 2009, **94**, 041903.
6 S. Chen, X. Gong, A. Walsh and S.-H. Wei, *Appl. Phys. Lett.*, 2010, **96**, 021902.
7 S. Chen, A. Walsh, X. G. Gong and S. H. Wei, *Adv. Mater.*, 2013, **25**, 1522–1539.
8 D. Shin, B. Saparov and D. B. Mitzi, *Adv. Energy Mater.*, 2017, **7**, 1602366.
9 T. Gokmen, O. Gunawan, T. K. Todorov and D. B. Mitzi, *Appl. Phys. Lett.*, 2013, **103**, 103506.
10 J. E. Moore, C. J. Hages, R. Agrawal, M. S. Lundstrom and J. L. Gray, *Appl. Phys. Lett.*, 2016, **109**, 021102.
11 S. Schorr, *Sol. Energy Mater. Sol. Cells*, 2011, **95**, 1482–1488.
12 S. Chen, L.-W. Wang, A. Walsh, X. Gong and S.-H. Wei, *Appl. Phys. Lett.*, 2012, **101**, 223901.
13 K. Biswas, S. Lany and A. Zunger, *Appl. Phys. Lett.*, 2010, **96**, 201902.
14 T. Zhu, W. P. Huhn, G. C. Wessler, D. Shin, B. Saparov, D. B. Mitzi and V. Blum, *Chem. Mater.*, 2017, **29**, 7868–7879.
15 J.-P. Sun, G. C. McKeown Wessler, T. Wang, T. Zhu, V. Blum and D. B. Mitzi, *Chem. Mater.*, 2020, **32**, 1636.
16 D. Shin, T. Zhu, X. Huang, O. Gunawan, V. Blum and D. B. Mitzi, *Adv. Mater.*, 2017, **29**, 1606945.
17 D. Shin, B. Saparov, T. Zhu, W. P. Huhn, V. Blum and D. B. Mitzi, *Chem. Mater.*, 2016, **28**, 4771–4780.
18 F. Hong, W. Lin, W. Meng and Y. Yan, *PCCP Phys. Chem. Chem. Phys.*, 2016, **18**, 4828–4834.
19 B. Teymur, Y. Zhou, E. Ngaboyamahina, J. T. Glass and D. B. Mitzi, *Chem. Mater.*, 2018, **30**, 6116–6123.
20 J. Ge, P. Koirala, C. R. Grice, P. J. Roland, Y. Yu, X. Tan, R. J. Ellingson, R. W. Collins and Y. Yan, *Adv. Energy Mater.*, 2017, **7**, 1601803.
21 D. Shin, E. Ngaboyamahina, Y. Zhou, J. T. Glass and D. B. Mitzi, *J. Phys. Chem. Lett.*, 2016, **7**, 4554–4561.
22 Y. Zhou, D. Shin, E. Ngaboyamahina, Q. Han, C. B. Parker, D. B. Mitzi and J. T. Glass, *ACS Energy Lett.*, 2017, **3**, 177–183.
23 M. Tampier and D. Johrendt, *Z. Anorg. Allg. Chem.*, 2001, **627**, 312–320.
24 G. C. Wessler, T. Zhu, J.-P. Sun, A. Harrell, W. P. Huhn, V. Blum and D. B. Mitzi, *Chem. Mater.*, 2018, **30**, 6566–6574.
25 T. Minemoto, T. Matsui, H. Takakura, Y. Hamakawa, T. Negami, Y. Hashimoto, T. Uenoyama and M. Kitagawa, *Sol. Energy Mater. Sol. Cells*, 2001, **67**, 83–88.
26 A. Crovetto, Z. Xing, M. Fischer, R. Nielsen, C. N. Savory, T. Rindzevicius, N. Stenger, D. O. Scanlon, I. Chorkendorff and P. C. Vesborg, *ACS Appl. Mater. Interfaces*, 2020, **12**, 50446–50454.
27 J.-P. Sun, J. A. Márquez, H. Stange, R. Mainz and D. B. Mitzi, *Phys. Rev. Mater.*, 2019, **3**, 055402.

28 D. B. Mitzi, M. Yuan, W. Liu, A. J. Kellock, S. J. Chey, V. Deline and A. G. Schrott, *Adv. Mater.*, 2008, **20**, 3657–3662.
29 T. K. Todorov, O. Gunawan, T. Gokmen and D. B. Mitzi, *Prog. Photovoltaics*, 2013, **21**, 82–87.
30 T. K. Todorov, K. B. Reuter and D. B. Mitzi, *Adv. Mater.*, 2010, **22**, E156–E159.
31 O. Gunawan, Y. Virgus and K. F. Tai, *Appl. Phys. Lett.*, 2015, **106**, 062407.
32 O. Gunawan and M. A. Pereira, *US Pat.*, 9772385, 2017.
33 O. Gunawan, S. R. Pae, D. M. Bishop, Y. Virgus, J. H. Noh, N. J. Jeon, Y. S. Lee, X. Shao, T. Todorov and D. B. Mitzi, *Nature*, 2019, **575**, 151–155.
34 S. Kim, K. M. Kim, H. Tampo, H. Shibata, K. Matsubara and S. Niki, *Sol. Energy Mater. Sol. Cells*, 2016, **144**, 488–492.
35 D. B. Khadka and J. Kim, *J. Phys. Chem. C*, 2015, **119**, 1706–1713.
36 C. M. Sutter-Fella, J. A. Stückelberger, H. Hagendorfer, F. La Mattina, L. Kranz, S. Nishiwaki, A. R. Uhl, Y. E. Romanyuk and A. N. Tiwari, *Chem. Mater.*, 2014, **26**, 1420–1425.
37 T. Gershon, B. Shin, N. Bojarczuk, M. Hopstaken, D. B. Mitzi and S. Guha, *Adv. Energy Mater.*, 2015, **5**, 1400849.
38 M. Johnson, S. Baryshev, E. Thimsen, M. Manno, X. Zhang, I. Veryovkin, C. Leighton and E. Aydil, *Energy Environ. Sci.*, 2014, **7**, 1931–1938.
39 B. Teymur, S. Levcenco, H. Hempel, E. Bergmann, J. A. Márquez, L. Choubrac, I. G. Hill, T. Unold and D. B. Mitzi, *Nano Energy*, 2020, **80**, 105556.
40 J. A. Márquez, J.-P. Sun, H. Stange, H. Ali, L. Choubrac, S. Schäfer, C. J. Hages, K. Leifer, T. Unold and D. B. Mitzi, *J. Mater. Chem. A*, 2020, **8**, 11346–11353.
41 D. Liao and A. Rockett, *Appl. Phys. Lett.*, 2003, **82**, 2829–2831.
42 T. Nakada and A. Kunioka, *Appl. Phys. Lett.*, 1999, **74**, 2444–2446.
43 C.-S. Jiang, F. Hasoon, H. Moutinho, H. Al-Thani, M. Romero and M. Al-Jassim, *Appl. Phys. Lett.*, 2003, **82**, 127–129.
44 S. Chichibu, T. Mizutani, K. Murakami, T. Shioda, T. Kurafuji, H. Nakanishi, S. Niki, P. Fons and A. Yamada, *J. Appl. Phys.*, 1998, **83**, 3678–3689.
45 R. Sharma and S. Rodriguez, *Phys. Rev.*, 1967, **153**, 823.
46 A. Crovetto, S. Kim, M. Fischer, N. Stenger, A. Walsh, I. Chorkendorff and P. C. Vesborg, *Energy Environ. Sci.*, 2020, **13**, 3489–3503.
47 W. Liu, R. Butté, A. Dussaigne, N. Grandjean, B. Deveaud and G. Jacopin, *Phys. Rev. B*, 2016, **94**, 195411.
48 D. Snoke, *Solid State Commun.*, 2008, **146**, 73–77.
49 H. Hempel, C. J. Hages, R. Eichberger, I. Repins and T. Unold, *Sci. Rep.*, 2018, **8**, 1–9.
50 C. J. Hages, A. Redinger, S. Levcenko, H. Hempel, M. J. Koeper, R. Agrawal, D. Greiner, C. A. Kaufmann and T. Unold, *Adv. Energy Mater.*, 2017, **7**, 1700167.
51 H. Hempel, A. Redinger, I. Repins, C. Moisan, G. Larramona, G. Dennler, M. Handwerg, S. F. Fischer, R. Eichberger and T. Unold, *J. Appl. Phys.*, 2016, **120**, 175302.
52 C. Zhang, J. Zhang, Y. Hao, Z. Lin and C. Zhu, *J. Appl. Phys.*, 2011, **110**, 064504.
53 S. S. Hegedus and W. N. Shafarman, *Prog. Photovoltaics*, 2004, **12**, 155–176.
54 F. Engelhardt, L. Bornemann, M. Köntges, T. Meyer, J. Parisi, E. Pschorr-Schoberer, B. Hahn, W. Gebhardt, W. Riedl and U. Rau, *Prog. Photovoltaics*, 1999, **7**, 423–436.
55 A. Nakane, H. Tampo, M. Tamakoshi, S. Fujimoto, K. M. Kim, S. Kim, H. Shibata, S. Niki and H. Fujiwara, *J. Appl. Phys.*, 2016, **120**, 064505.
56 K. Sardashti, R. Haight, T. Gokmen, W. Wang, L. Y. Chang, D. B. Mitzi and A. C. Kummel, *Adv. Energy Mater.*, 2015, **5**, 1402180.
57 W. Shockley and H. J. Queisser, *J. Appl. Phys.*, 1961, **32**, 510–519.

 